Rapid glacier retreat rates observed in West Antarctica

Article *in* Nature Geoscience · January 2022

DOI: 10.1038/s41561-021-00877-z

8 authors, including:

Pietro Milillo
University of Houston
90 PUBLICATIONS **1,350** CITATIONS
SEE PROFILE

E. Rignot
University of California, Irvine
549 PUBLICATIONS **34,755** CITATIONS
SEE PROFILE

Paola Rizzoli
German Aerospace Center (DLR)
195 PUBLICATIONS **1,424** CITATIONS
SEE PROFILE

Jeremie Mouginot
University of California, Irvine
154 PUBLICATIONS **11,505** CITATIONS
SEE PROFILE

nature geoscience

ARTICLES

https://doi.org/10.1038/s41561-021-00877-z

Rapid glacier retreat rates observed in West Antarctica

P. Milillo[1,2,3]✉, E. Rignot[2,4,5], P. Rizzoli[3], B. Scheuchl[2], J. Mouginot[6], J. L. Bueso-Bello[3], P. Prats-Iraola[3] and L. Dini[7]

The Pope, Smith and Kohler glaciers, in the Amundsen Sea Embayment of West Antarctica, have experienced enhanced ocean-induced ice-shelf melt, glacier acceleration, ice thinning and grounding-line retreat in the past 30 years. Here we present observations of the grounding-line retreat of these glaciers since 2014 using a constellation of interferometric radar satellites combined with precision surface elevation data. We find that the grounding lines develop spatially variable, kilometre-scale, tidally induced migration zones. After correction for tidal effects, we detect a sustained pattern of retreat coincident with high melt rates of ungrounded ice, marked by episodes of more rapid retreat. In 2017, Pope Glacier retreated 3.5 km in 3.6 months, or 11.7 km yr^{-1}. In 2016–2018, Smith West retreated at 2 km yr^{-1} and Kohler at 1.3 km yr^{-1}. While the retreat slowed in 2018–2020, these retreat rates are faster than anticipated by numerical models on yearly timescales. We hypothesize that the rapid retreat is caused by unrepresented, vigorous ice–ocean interactions acting within newly formed cavities at the ice–ocean boundary.

The Amundsen Sea Embayment (ASE) sector of West Antarctica, which includes the Pine Island, Thwaites, Haynes, Pope, Smith and Kohler glaciers, dominates the present-day contribution to sea-level rise from Antarctica[1,2]. Their ice volume above flotation is equivalent to a 1.2 m global sea-level rise. Located on the western flank of the ASE, the Pope, Smith and Kohler glaciers drain 7% of the ASE into the Crosson and Dotson ice shelves but contribute 24% of the total loss from ASE, with an average 32 Gt yr^{-1} mass loss (1 Gt = 10^9 ton = 10^{12} kg) during the period 1979–2017[2,3] (Fig. 1). Although their combined ice discharge is three times lower than that of the neighbouring Pine Island and Thwaites glaciers, their rapid speed up and retreat rate, along mostly retrograde bed slopes (bed elevation drops in the inland direction), are diagnostic of what an extensive glacier retreat associated with a 'marine ice-sheet instability' may look like in the broader remainder of West Antarctica in the future[4].

A number of changes were noted in previous studies of these glaciers. At the grounding line (where ice detaches from the bed and becomes afloat), the velocity of Pope Glacier increased from 370 m yr^{-1} in 1989 to 775 m yr^{-1} in 2016, which doubled its ice discharge from 5.5 ± 0.6 to 9.5 ± 0.7 Gt yr^{-1} (ref. [5]). Near the grounding line, grounded ice thinned at 9 m yr^{-1} between 2003 and 2008 while floating ice melted at 40 m yr^{-1} (refs. [6–8]). The grounding line retreated at 0.64 km yr^{-1} from 1996 to 2014[5]. On Smith East and West, the velocity increased by 280% (710 m yr^{-1}) and 370% (800 m yr^{-1}), respectively, in 1992–2015, which tripled their combined ice discharge as the grounding line retreated into thicker ice[5]. Between 2002 and 2009, Smith West thinned at 7 m yr^{-1} on grounded ice and melted at 70 m yr^{-1} on floating ice[9]. From 1992 to 2016, the grounding line of Smith West retreated at 2 km yr^{-1}, which was the fastest retreat rate in Antarctica[10], while Smith East retreated at 0.5 km yr^{-1}. By contrast, Kohler exhibited no speed up between 1994 and 2016, and its grounding line migrated back and forth between 1996 and 2014[5].

Short-term grounding-line variability

In this article, we present a new time series of one-day repeat synthetic aperture radar interferometry (InSAR) observations from the COSMO-SkyMed (CSK) constellation to survey the Pope, Smith East and West, and Kohler glaciers multiple times a year and update on their grounding-line position since year 2014. We combine the CSK differential InSAR (DInSAR) data (Supplementary Fig. 1) with time-tagged TanDEM-X (TDX) digital elevation models (DEMs) of the ice surface. The time series of DInSAR data reveals the temporal evolution of the grounding line caused by tidally induced migrations on top of a long-term grounding-line retreat (Methods)[11,12] (Fig. 1). The TDX DEMs (Supplementary Figs. 2 and 3) quantify temporal changes in ice surface elevation caused by changes in ice flow dynamics and surface mass balance on grounded ice, and additionally by bottom ice melt by the ocean waters on floating ice (Supplementary Fig. 3). In the DInSAR technique, we form the difference between a first one-day InSAR pair that includes signal associated with the nearly steady horizontal motion of the glacier and the tidal-dependent vertical tidal motion of the floating ice with a second one-day InSAR pair, acquired within 1 to 4 of 16-day cycles later, to eliminate the steady, horizontal motion of the glacier and detect the residual pattern of tidal motion. The DInSAR technique combines four SAR images from four epochs to image a differential pattern of tidal motion. We posit that the vertical motion detected farthest inland in the DInSAR data corresponds to the most positive (upward) tide, h_{max}, among the four epochs because the high tide will lift the glacier farther off the bed and allow seawater to intrude farther inland beneath the glacier, whereas low tide will force the grounding line to re-advance[12]. We model the tidal heights at the time of passage of the satellites using the Circum-Antarctic Tidal Simulation (CATS2008)[13] and correct the results for changes in atmospheric pressure. We examine the relationship between observed grounding-line position from each DInSAR element and

[1]Department of Civil and Environmental Engineering, University of Houston, Houston, TX, USA. [2]Department of Earth System Science, University of California, Irvine, CA, USA. [3]German Aerospace Center (DLR), Microwaves and Radar Institute, Munich, Germany. [4]Department of Civil and Environmental Engineering, University of California, Irvine, CA, USA. [5]Jet Propulsion Laboratory, California Institute of Technology, Pasadena, CA, USA. [6]Univ. Grenoble Alpes, CNRS, IRD, Grenoble INP, IGE, Grenoble, France. [7]Italian Space Agency (ASI), Matera, Italy. ✉e-mail: pmilillo@uh.edu

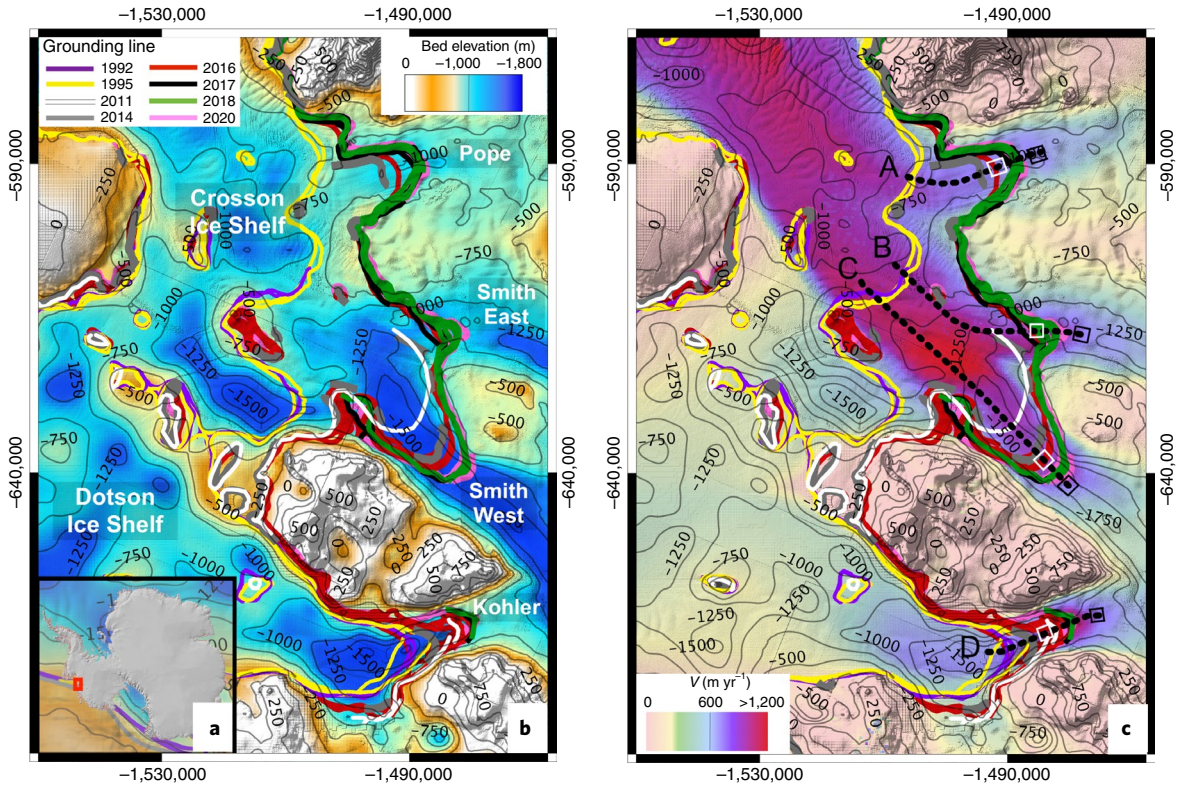

Fig. 1 | Pope, Smith East and West, and Kohler glaciers, West Antarctica. a, Location map in West Antarctica (red box). **b**, Shaded-relief bed elevation colour coded from −1,800 m (blue) to 0 m (brown) with 500 m contour levels (grey)[14,15] and grounding zones colour coded from 1992 to 2020. Retreat rates are shown in Figs. 2 and 3 along profiles A–D. **c**, Ice surface speed in 2016–2017, colour coded from brown to red. Black and white boxes near the 2016 grounding lines are used to calculate dynamic thinning and bottom ice melt in Fig. 4. Maps in **b** and **c** are represented in Antarctic projection.

Table 1 | Sensitivity of the grounding-line position to h_{max} for Pope, Smith East, Smith West and Kohler glaciers at different times, as a function of surface slope, bed slope and flotation factor relative to the 1996 grounding-line position and grounding-zone width

Glacier	Time (year)	a	GL retreat (km)	α (%)	β (%)	γ	GZ width (km)
Pope	2017	4.5 ± 2.1	3.50 ± 0.4	3	2.7	0.0050	1.5 ± 0.5
Longitude: 111.59° W	2018	1.1 ± 0.7	4.28 ± 0.4	3	3.0	0.0050	1.2 ± 0.5
Latitude: 75.27° S	2020	1.0 ± 0.7	4.25 ± 0.4	3	3.5	0.0050	1.4 ± 0.5
Smith East	2017	16.0 ± 2.1	0 ± 0.4	1.4	3.0	0.0150	2.4 ± 0.5
Longitude: 112.40° W	2018	12.5 ± 2.5	2.35 ± 0.4	1.4	3.0	0.0150	1.9 ± 0.5
Latitude: 75.18° S	2020	10.1 ± 2.1	3.25 ± 0.4	1.7	2.4	0.0180	1.7 ± 0.5
Smith West	2016	20.1 ± 10	0 ± 0.3	0.5	0.4	0.0053	2.7 ± 0.5
Longitude: 112.78° W	2017	9.8 ± 6	3.00 ± 0.4	1.4	1.1	0.0140	2.4 ± 0.5
Latitude: 75.15° S	2018	14.7 ± 6	4.50 ± 0.4	1.4	0.8	0.0130	2.4 ± 0.5
	2020	6.1 ± 6	4.00 ± 0.4	1.5	0.2	0.0130	2.5 ± 0.5
Kohler	2016	5.6 ± 4	0 ± 0.5	0.5	3.3	0.0330	1.9 ± 0.5
Longitude: 114.17° W	2018	21.1 ± 7.5	2.30 ± 0.4	1.3	3.7	0.0150	1.8 ± 0.5
Latitude: 75.10° S	2020	37.2 ± 7.6	2.50 ± 0.4	3.2	4.2	0.0330	1.7 ± 0.5

For ice in hydrostatic equilibrium on a hard bed, we expect $a = GL/(h_{max}/\gamma) = 1$. a, amplification factor; GL, grounding line; α, surface slope; β, bed slope; γ, flotation factor; GZ, grounding zone.

the modelled maximum tide (h_{max}) at the time of passage of the satellites (Fig. 2).

We find a larger-than-expected variability in grounding-line position as a function of tide. On Smith West, the grounding line migrates at tidal frequencies over a 3-km-wide grounding zone (where the grounding line migrates with changes in oceanic tide) in 2016–2017. In 1992–1995, the grounding zone was 1.6 km wide (Fig. 3). The larger tidally induced grounding zone in 2016–2017 is con-

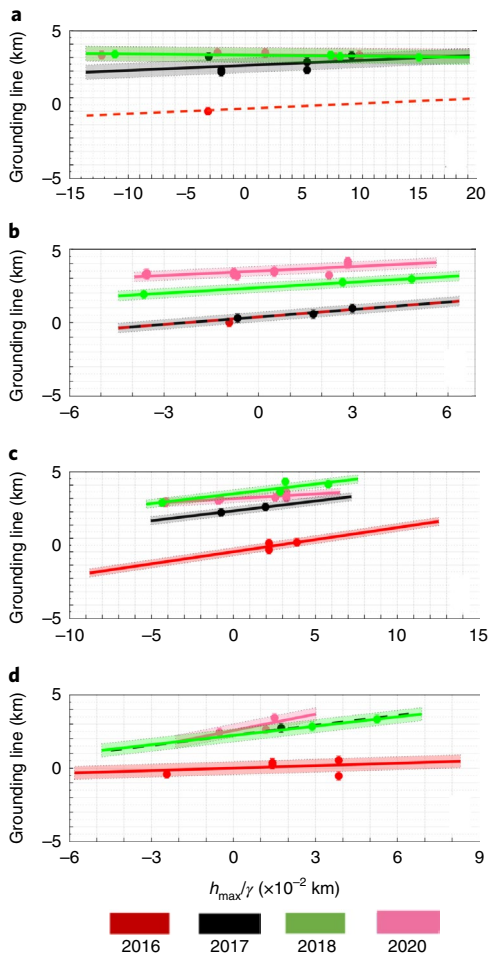

Fig. 2 | Grounding Line migration as a function of tides and glacier geometry. a–d, Tidally induced grounding-line migration and secular retreat rates at Pope (**a**), Smith East (**b**), Smith West (**c**) and Kohler (**d**) glaciers as a function of h_{max} among the four epochs of the DInSAR data divided by the γ values deduced from local, time-dependent surface and bed slopes (Table 1). Grounding-line migration is measured along profiles aligned with the flow direction and referenced to the 2016 mean sea-level grounding-line position. Coloured lines are linear regressions of grounding line versus h_{max}/γ. Shaded areas correspond to a 1σ uncertainty. When only one grounding-line measurement is available for a given year (for example, Pope and Smith East in 2016/Kohler in 2017), a dashed red/black line is used assuming the same regression slope as for the nearest available year (2017 or 2018).

sistent with a flatter bed topography at that location[14,15] compared with 1992–1995 (Fig. 3). A flatter topography favours intrusion of pressurized seawater at the glacier bed at high tide over a larger area. Conversely, the grounding zone will be narrower along steeper parts of the bed (for example, along the side margins or at bed peaks; Fig. 1), if tidal migration is controlled by hydrostatic equilibrium[11,12].

We find a positive linear relationship between observed grounding-line position and modelled h_{max} (Fig. 2). The slope of the regression varies from glacier to glacier and is time dependent as the grounding line retreats to a different bed position (Table 1). If we assume flotation, the sensitivity of the grounding-line position to tidal height, γ, is given by the bed and surface slopes and the density of seawater and ice (Methods). We find, however, that the observed grounding-line migration is amplified by a factor, a, that varies from 1 to 37 (Table 1); that is, the migration is one order of magnitude larger than expected from flotation. Within the grounding zones of Pope, Smith and Kohler glaciers, we find that ice deviates from flotation by only 3.9 ± 6 m, 2.5 ± 8 m and 2.2 ± 6 m, respectively (Supplementary Fig. 5).

Long-term grounding-line migration

We employ the empirical relationship between grounding-line position and tidal height to derive a mean, or tidal-corrected, position of grounding line at different epochs and in turn use these results to determine the longer-term (months to years) migration independent of the tidal state (Fig. 3). We find that the grounding line of Smith East retreated at 1.4 km yr^{-1} in 2011–2016 along a relatively flat bed, or three times faster than in 1996–2011[5]. The grounding line remained stable in 2016–2017 at a transition to prograde slopes, followed by a retreat at 2.4 km yr^{-1} in 2017–2018 and a slow down to 0.9 km yr^{-1} in 2018–2020 along steeper prograde slopes (Fig. 3). The grounding line of Smith West retreated 3.0 ± 0.4 km in 2016–2017 and 1.5 ± 0.4 km in 2017–2018; it remained stable in 2018–2020, for an average 0.9 km yr^{-1} retreat in 2016–2020, or 50% slower than in 1992–2011 (Fig. 3). During 2014–2020, the retreat proceeded on a nearly flat bed whereas in 1996–2011, the grounding line retreated along retrograde slopes (600 m drop in elevation over 30 km). On the western flank of Smith West (Point D in Supplementary Fig. 3), 11 km^2 of grounded ice disappeared between February 2016 and December 2017, accompanied by a 2.3 km yr^{-1} retreat of the grounding line.

To the east, Pope Glacier retreated 2.7 ± 0.8 km in 2014–2016, or 1.3 km yr^{-1}, versus 0.6 km yr^{-1} in 1994–2014[5]. The grounding zone is only 1 km wide (Fig. 3). In January–May 2017, over a period of only 113 days, the grounding line retreated 3.5 ± 0.8 km (Methods), or 11.7 km yr^{-1}. The grounding line subsequently retreated at 0.8 km yr^{-1} in 2017–2018 and remained stable in 2018–2020 as the grounding line transitioned to prograde bed slopes, which extend another 20 km inland. During 2016–2020, the grounding line averaged a retreat rate of 1 km yr^{-1}.

To the west, Kohler Glacier exhibits a 2-km-wide grounding zone along prograde bed slopes (Fig. 3). The grounding line retreated 2.3 ± 0.4 km in 2016–2018 but did not retreat in 2018–2020, for an average 0.5 km yr^{-1} retreat in 2016–2020, or 60% higher than in 1995–2016. A previous study suggested a re-advance of the grounding line in 2011–2014[5]. The grounding line now stands 7 km away from Smith West and 2 km from retrograde slopes. At the current rate, the two glaciers will merge within the next 15 years. This merger will have two implications. First, the connection of ice-shelf cavities will change the ocean circulation beneath Dotson[16]. Second, the prograde bed slopes of Kohler, which explained its apparent stability in 1992–2014, did not stop the retreat. Similarly, Smith East retreated slowly along prograde slopes in 2017–2020.

Retreat rates of 3 km yr^{-1} on Smith West in 2016–2017, 2.4 km yr^{-1} on Smith East in 2017–2018, 11.7 km yr^{-1} in three months on Pope in 2017 and 2.3 km yr^{-1} on Kohler in 2016–2018 are large compared with those observed on other glaciers in Antarctica and Greenland. The grounding line of Jakobshavn Isbræ, central west Greenland, retreated at 0.5 km yr^{-1} in 2002–2016, with a brief 3.8 km jump in 2011–2012[17]. Zachariae Isstrøm, northeast Greenland, retreated at 0.55 km yr^{-1} in 2014–2019[18,19]. Helheim retreated 4 km between August 2004 and August 2005[20] but partially re-advanced in subsequent years. In West Antarctica, Thwaites has retreated 1 km yr^{-1} on average since 1992, similar to Pine Island[11,12,21,22]. The observed high retreat rates of Smith, Pope and Kohler in recent years are, however, consistent with retreat rates as large as 5 to 10 km yr^{-1} inferred recently for former palaeo ice streams[23], giving credence to the fact that glaciers can retreat at speeds of several kilometres per year.

Ice–ocean interactions in the grounding zones

The time series of DEMs document the rate of ice thinning accompanying the retreat. The highest thinning rates are observed in areas of freshly ungrounded ice[6,7] and are caused by a combination

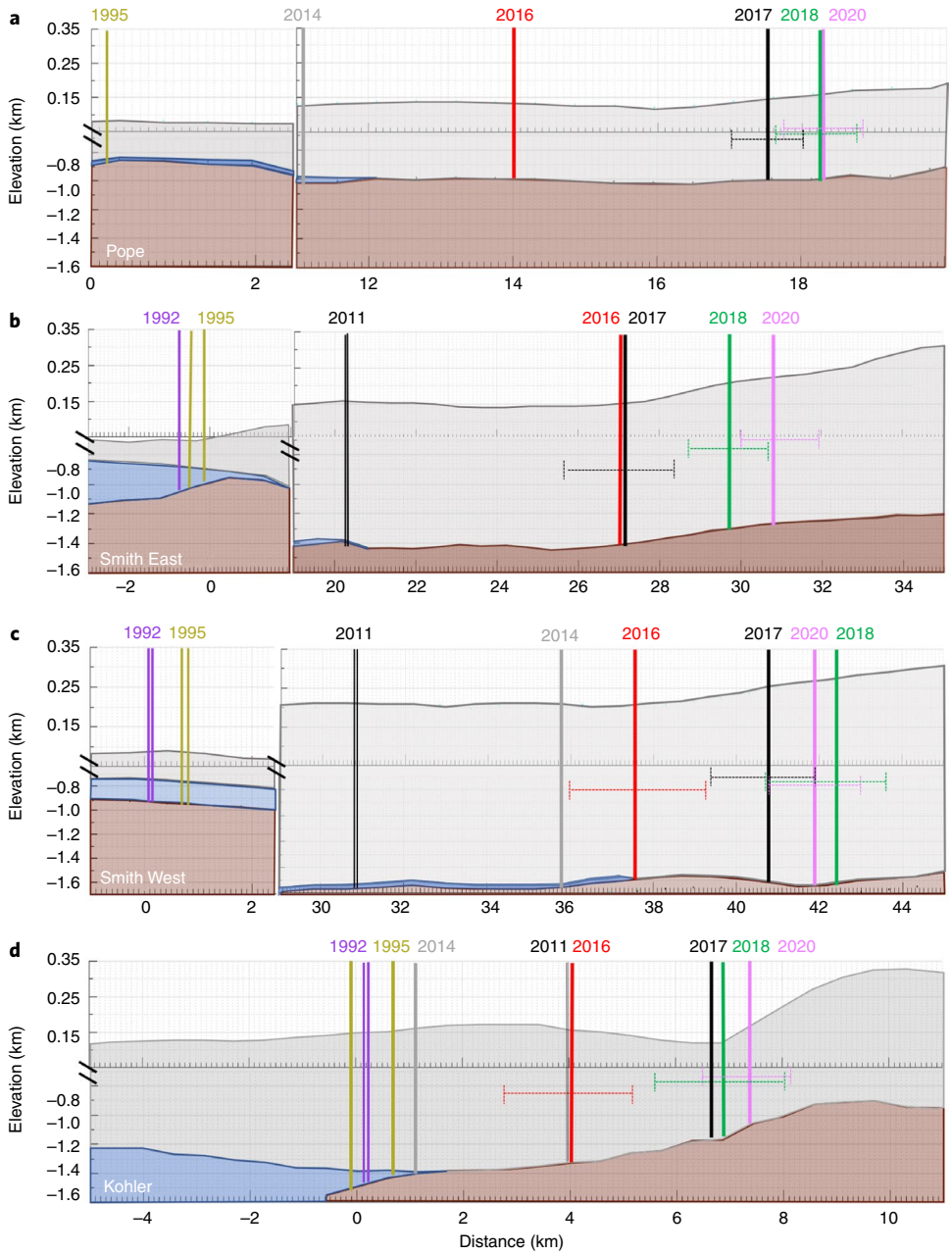

Fig. 3 | Pope, Smith and Kohler glaciers profiles. a–d, Surface and bed profiles of Pope (**a**), Smith East (**b**), Smith West (**c**) and Kohler (**d**) glaciers for year 2011 from BedMachine[14] centred at the grounding zone of each glacier (Fig. 1). Solid-coloured lines mark the grounding zone at zero tide, and error bars mark the width of the grounding zone deduced from Fig. 2. Grounding zones in 1995, 2011 and 2014 from ref. [5] are not corrected for tide due to a limited set of repeat observations. The reference position is the grounding line from the 1990s (Fig. 1). Distance is from north (left) to south (right) in kilometres.

of dynamic thinning and bottom melt by the ocean waters (surface mass balance is less than 0.5 m yr^{-1} in this region[25], hence is not a factor). On land, dynamic thinning equals the rate of ice thinning, which we calculate over grounded ice adjacent to the freshly ungrounded ice (Fig. 1). We assume that the same rate of dynamic thinning applies on ungrounded ice, subtract this rate from the observed rate of ice thinning, assume hydrostatic equilibrium and deduce the resulting bottom melt rate (Methods). Ice deviates from flotation by only a few metres due to bending stresses[11,24] in these regions. Above the 2020 grounding lines, we detect ice thinning at 4 to 7 m yr^{-1} on Pope, Smith and Kohler glaciers (Fig. 4) and peak values of 9 m yr^{-1} on Smith West in 2011–2014 (Supplementary Fig. 3). For ice that ungrounded on Pope in 2014–2017, we calculate a bottom melt rate of 86 ± 9 m yr^{-1} (Fig. 4a and Supplementary Figs. 5 and 6). On Smith East, dynamic thinning of 5 m yr^{-1} in 2011–2019 on grounded ice translates into a melt rate of 22 ± 6 m yr^{-1} on freshly ungrounded ice (Fig. 4b). For Smith West, grounded ice thinning at 6 ± 0.4 m yr^{-1} yields a 65 ± 6 m yr^{-1} melt rate of ungrounded ice. For Kohler, grounded ice thinning at 3–4 m yr^{-1} yields 19 ± 7 m yr^{-1} melting of ungrounded ice. At select locations D and E (Supplementary Fig. 3) on Smith West, inferred bottom melt rates exceed 100 m yr^{-1}, for example, 140 m yr^{-1} in 2016–2017 at D. On Kohler, the melt rate is 100 ± 9 m yr^{-1} in 2016–2019 at point F (Supplementary Fig. 3). These melt rates are high compared with melt rates observed on the ice shelf proper[26] and in the upper range of values employed in numerical ice-sheet models[9,27–29].

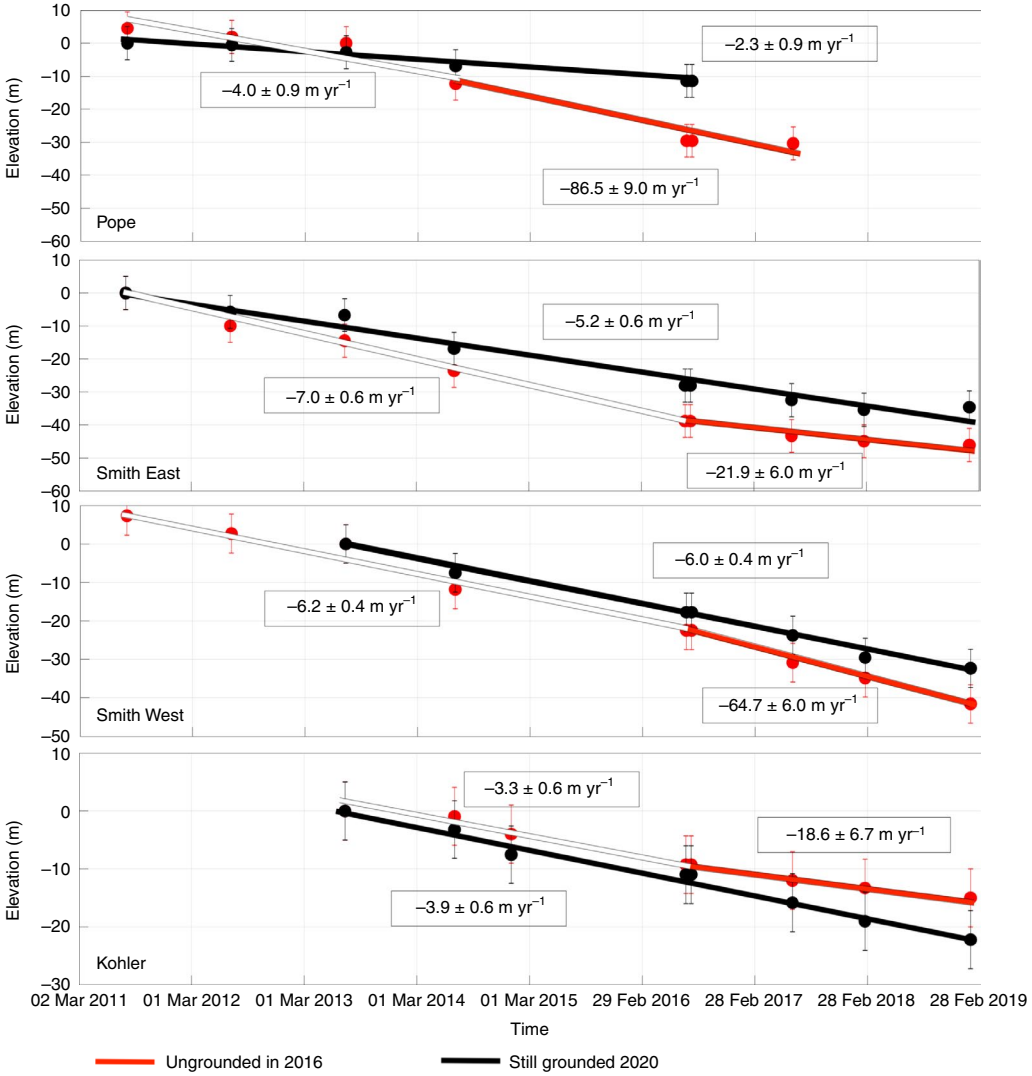

Fig. 4 | Rate of ice thickness change time series. Rate of ice thickness change, $\frac{dh}{dt_{pre}}$, and melt rate, m_b, of West Antarctic glaciers and their relative error bars deduced from a time series of TDX digital elevation data corrected for firn depth (Supplementary Fig. 3). Black lines correspond to black boxes in Fig. 1 on grounded ice. White lines correspond to white boxes in Fig. 1 where ice transitioned from grounded to floating during the period (marked by a colour change from white to red). Other examples are shown in Supplementary Fig. 3 with the same approach.

When similar high melt rates are used to force models, the model results can match the observed retreat, except for Kohler where the modelled grounding line remains stable[9]. As noted in previous studies[9,30], elevated ice melt near the grounding line is an additional constraint on the speed of retreat. Wider grounding zones are explainable by the presence of a deformable bed[31] or the propagation of elastic cracks forced by pressurized seawater[32,33]. Intrusion of pressurized seawater in the sub-glacial cavities will melt grounded ice and reduce basal resistance[34]. Numerical models indicate that the inclusion of ice melt within a grounding zone significantly increases the speed of retreat[30]. Other modelling studies even emphasize that it is not possible to match the observed retreat if ice melt processes are not included in the grounding zone[9,28].

The Pope, Smith East and West, and Kohler glaciers control a drainage area with an ice volume above flotation equivalent of 6 cm global sea-level rise, which is small, so the risks of rapid sea-level rise from this sector of West Antarctica are low. Yet the physical processes driving their retreat are the same that operate on neighbouring Thwaites and Pine Island, which hold a 1.2 m global sea-level rise and may destabilize the rest of West Antarctica. Understanding the physical processes driving the fast retreat of Pope, Smith and Kohler, especially the magnitude of ice melt in the grounding zones, is therefore critical to explain and reproduce the observed rates of retreat. The results will in turn help reduce uncertainties in the upper bounds of maximum contribution to sea-level rise from West Antarctica in decades to come.

Online content

Any methods, additional references, Nature Research reporting summaries, source data, extended data, supplementary information, acknowledgements, peer review information; details of author contributions and competing interests; and statements of data and code availability are available at https://doi.org/10.1038/s41561-021-00877-z.

Received: 28 July 2020; Accepted: 16 November 2021;
Published online: 13 January 2022

References

1. Shepherd, A. et al. Mass balance of the Antarctic Ice Sheet from 1992 to 2017. *Nature* **558**, 219–222 (2018).

2. Rignot, E. et al. Four decades of Antarctic Ice Sheet mass balance from 1979–2017. *Proc. Natl Acad. Sci. USA* **116**, 1095–1103 (2019).
3. Mouginot, J., Rignot, E. & Scheuchl, B. Sustained increase in ice discharge from the Amundsen Sea Embayment, West Antarctica, from 1973 to 2013. *Geophys. Res. Lett.* **41**, 1576–1584 (2014).
4. Schoof, C. Marine ice sheet stability. *J. Fluid Mech.* **698**, 62–72 (2012).
5. Scheuchl, B., Mouginot, J., Rignot, E., Morlighem, M. & Khazendar, A. Grounding line retreat of Pope, Smith, and Kohler glaciers, West Antarctica, measured with Sentinel-1a radar interferometry data. *Geophys. Res. Lett.* **43**, 8572–8579 (2016).
6. Lilien, D. A., Joughin, I., Smith, B. & Shean, D. E. Changes in flow of Crosson and Dotson ice shelves, West Antarctica, in response to elevated melt. *Cryosphere* **12**, 1145–1431 (2018).
7. Gourmelen, N. et al. Channelized melting drives thinning under a rapidly melting Antarctic ice shelf. *Geophys. Res. Lett.* **44**, 9796–9804 (2017).
8. Khazendar, A. et al. Rapid submarine ice melting in the grounding zones of ice shelves in West Antarctica. *Nat. Comm.* **7**, 13243 (2016).
9. Lilien, D. A., Joughin, I., Smith, B. & Gourmelen, N. Melt at grounding line controls observed and future retreat of Smith, Pope, and Kohler glaciers. *Cryosphere* **13**, 2817–2834 (2019).
10. Konrad, H. et al. Net retreat of Antarctic glacier grounding lines. *Nat. Geosci.* **11**, 258–262 (2018).
11. Milillo, P. et al. Heterogeneous retreat and ice melt of Thwaites Glacier, West Antarctica. *Sci. Adv.* **5**, eaau3433 (2019).
12. Milillo, P. et al. On the short-term grounding zone dynamics of Pine Island Glacier, West Antarctica, observed with COSMO-SkyMed Interferometric Data. *Geophys. Res. Lett.* **44**, 10436–10444 (2017).
13. Padman, L., Fricker, H. A., Coleman, R., Howard, S. & Erofeeva, L. A new tide model for the Antarctic ice shelves and seas. *Ann. Glaciol.* **34**, 247–254 (2002).
14. Millan, R., Rignot, E., Bernier, V., Morlighem, M. & Dutrieux, P. Bathymetry of the Amundsen Sea Embayment sector of West Antarctica from operation IceBridge gravity and other data. *Geophys. Res. Lett.* **44**, 1360–1368 (2017).
15. Morlighem, M. et al. Deep glacial troughs and stabilizing ridges unveiled beneath the margins of the Antarctic ice sheet. *Nat. Geosci.* **13**, 132–137 (2019).
16. Miles, R. et al. Glider observations of the Dotson Ice Shelf outflow. *Deep Sea Res. 2* **123**, 16–29 (2016).
17. An, L. et al. Bed elevation of Jakobshavn Isbræ, West Greenland, from high-resolution airborne gravity and other data. *Geophys. Res. Lett.* **44**, 3728–3736 (2017).
18. Mouginot, J. et al. Fast retreat of Zachariæ Isstrøm, northeast Greenland. *Science* **350**, 1357–1361 (2015).
19. An, L. et al. Ocean melting of the Zachariae Isstrom and Nioghalvfjerdsfjorden glaciers, northeast Greenland. *Proc. Natl Acad. Sci. USA* **118**, e2015483118 (2021).
20. Howat, I. M., Joughin, I., Tulaczyk, S. & Gogineni, S. Rapid retreat and acceleration of Helheim Glacier, east Greenland. *Geophys. Res. Lett.* **32**, 22 (2005).
21. Rignot, E., Mouginot, J., Morlighem, M., Seroussi, H. & Scheuchl, B. Widespread, rapid grounding line retreat of Pine Island, Thwaites, Smith, and Kohler glaciers, West Antarctica, from 1992 to 2011. *Geophys. Res. Lett.* **41**, 3502–3509 (2014).
22. DeConto, R. M. & Pollard, D. Contribution of Antarctica to past and future sea-level rise. *Nature* **531**, 591–597 (2016).
23. Dowdeswell, J. A. et al. Delicate seafloor landforms reveal past Antarctic grounding-line retreat of kilometers per year. *Science* **368**, 1020–1024 (2020).
24. Yu, H., Rignot, E., Seroussi, H., Morlighem, M. & Choi, Y. Impact of iceberg calving on the retreat of Thwaites Glacier, West Antarctica over the next century with different calving laws and ocean thermal forcing. *Geophys. Res. Lett.* **46**, 14539–14547 (2019).
25. van Wessem, J. M. et al. Modelling the climate and surface mass balance of polar ice sheets using RACMO2—part 2: Antarctica (1979–2016). *Cryosphere* **12**, 1479–1498 (2018).
26. Rignot, E., Jacobs, S., Mouginot, J. & Scheuchl, B. Ice-shelf melting around Antarctica. *Science* **341**, 266–270 (2013).
27. Joughin, I., Smith, B. E. & Medley, B. Marine ice sheet collapse potentially under way for the Thwaites Glacier Basin, West Antarctica. *Science* **344**, 735–738 (2014).
28. Goldberg, D. N., Gourmelen, N., Kimura, S., Millan, R. & Snow, K. How accurately should we model ice shelf melt rates? *Geophys. Res. Lett.* **46**, 189–199 (2019).
29. Seroussi, H. et al. Continued retreat of Thwaites Glacier, West Antarctica, controlled by bed topography and ocean circulation. *Geophys. Res. Lett.* **44**, 6191–6199 (2017).
30. Seroussi, H. & Morlighem, M. Representation of basal melting at the grounding line in ice flow models. *Cryosphere* **12**, 3085–3096 (2018).
31. Sayag, R. & Worster, M. G. Elastic dynamics and tidal migration of grounding lines modify subglacial lubrication and melting. *Geophys. Res. Lett.* **40**, 5877–5881 (2013).
32. Tsai, V. C. & Gudmundsson, G. H. An improved model for tidally modulated grounding-line migration. *J. Glaciol.* **61**, 216–222 (2015).
33. Begeman, C. B. et al. Tidal pressurization of the ocean cavity near an Antarctic ice shelf grounding line. *J. Geophys. Res. Oceans* **125**, e2019JC015562 (2020).
34. Reese, R., Winkelmann, R. & Gudmundsson, H. Grounding-line flux formula applied as a flux condition in numerical simulations fails for buttressed Antarctic ice streams. *Cryosphere* **12**, 3229–3242 (2018).

Methods

CSK grounding-line analysis. We survey the Pope, Smith and Kohler glaciers grounding lines using the CSK constellation. The acquisition campaign includes two phases: at the time of phase one (2016–2018), CSK included four low-orbit satellites carrying an X-band SAR (3.1 cm wavelength) at HH polarization (horizontal transmit and receive). Each satellite has a 16-day repeat cycle. Shorter temporal baselines are achieved using the constellation. We use interferometric acquisitions spanning one-day time interval with the satellites CSK2 and CSK3 (Supplementary Fig. 4). In 2019, no data could be acquired due to a change in satellites configuration and the addition of four more satellites, including two X-band COSMO-SkyMed second generation and two SAOCOM satellites at L-band. Phase two started in 2020, and acquisition spanning one-day intervals restarted using the CSK2 and CSK4 satellites (Supplementary Fig. 4). Here, we analyse scenes in single-look complex mode covering a 40×40 km swath from three different tracks, at 3 m spacing in the azimuth (along-track) and range (cross-track) directions. CSK SAR interferograms are assembled by concatenating 4×CSK STRIPMAP consecutive frames. The incidence angle averages 21° across the swath. We apply eight looks (number of elements averaged together to reduce noise) in both the range and azimuth directions to improve phase coherence. We use orbit information and pixel offsets to maximize coherence between image pairs. Given the large interferometric baseline characterizing CSK2/3 interferometric pairs, we remove the topographic component of the interferometric phase using time-tagged TDX DEMs acquired closest in time with the CSK data[11]. The interferometric baseline is much reduced in phase 2 of this project (less than 100 m), in which case we used the same TDX DEM from 2019 with all data. A grounding-line measurement is formed by differencing the two one-day interferograms. We use 216 stripmap data (an average of 54 single-look complexes per year) divided in 3 tracks (18 images composed by 4 frames per image) acquired between February 2016 and November 2020 to produce 26 differential interferograms (DInSAR), which reveal vertical tidal displacements and other transient motion of the ice, for example, subsidence/rise of the ice surface with lake drainage/filling (Supplementary Fig. 1). The precision of detection of the grounding line is greater when the differential tidal signal is larger and typically of the order of 100–200 m (refs. [11,12]). We select 22 DInSAR pairs (85% of the total number of pairs) (Supplementary Fig. 1) that display sufficient tidal signal (differential tidal signal larger than 4.5 cm corresponding to three interferometric fringes in the line of sight at X band), acquired no more than two months apart to avoid contaminating the vertical signal with seasonal velocity changes. The grounding line is manually picked near the most inland interferometric fringe associated with tidal motion. We verify that in each DInSAR frame we count the same number of fringes across the flexure zone (the zone of concentrated fringes where ice adjusts to hydrostatic equilibrium across the grounding line). Using multiple grounding-line measurements, we identify a grounding zone (where the grounding line migrates back and forth with changes in oceanic tide) (Supplementary Fig. 1).

One grounding-line measurement combines data acquired at four different times. We expect the grounding line to migrate inland at high tide and seaward at low tide. We posit that the most retreated position of the grounding line corresponds to the most positive (upwards) tidal displacement among the four epochs, h_{max}. We calculate the tidal amplitude using tide predictions from the CATS2008 model with a precision of 5 cm (ref. [13]) (Supplementary Table 1). Inverse barometer effect is also taken into consideration following the same approach described in ref. [36] using European Centre for Medium-Range Weather Forecasts Re-analysis Interim data[37](Supplementary Table 2). Across the grounding zone, we calculate an average surface slope, α, from the TDX DEM and a bed slope, β, from BedMachine Antarctica[13,14] along the flow direction (Supplementary Fig. 3) with a length scale of 3 km and calculate a sensitivity parameter γ as:

$$\gamma = \left(1 - \frac{\rho_i}{\rho_w}\right)\beta + \frac{\rho_i}{\rho_w}\alpha \quad (1)$$

where $\rho_i = 917\,kg\,m^{-3}$ and $\rho_w = 1{,}027\,kg\,m^{-3}$ are, respectively, the density of ice and seawater. At flotation, when the tide changes by dh^+, the grounding line should migrate inland by $dGL = dh^+/\gamma$ on a rigid bed based on hydrostatic equilibrium (that is, with $dh^+ = 1$ m and $\gamma = 0.01$ we expect dGL to be 100 m). The most inland position of the grounding line verifies $dGL_{max} = h_{max}/\gamma$. In reality, however, because of visco-elastic bed deformation and tidal pressure[30,31], the migration is amplified by a factor a: $dGL_{max} = a\,h_{max}/\gamma$ (Fig. 2). The inferred values of the amplification factor, a, are listed in Table 1.

TDX bed topography and height above flotation in Antarctica. We generate a time series of 241 time-tagged DEMs using the global TDX product[35] for geocoding and calibration for the period 2011–2019. The SAR processing chain comprises six steps: (1) spaceborne monostatic TerraSAR-X processing, (2) bistatic TDX processing, (3) interferometric combination of images, (4) phase unwrapping, (5) phase-to-height conversion and (6) geocoding to a latitude/longitude grid. Using Airborne Topographic Mapper data over grounded ice, we estimate a relative height accuracy of 2.1 m (Supplementary Fig. 2). For calculating the height above flotation, h_f, we use surface elevation above mean sea level, h_{dem}, and ice-equivalent thickness, H_i, from BedMachine Antarctica[14,15] that combines ice thickness derived from airborne radar depth sounders with InSAR-derived ice velocity and RACMO2.3 surface mass balance data[25]. On floating ice, h_{dem} is corrected with a firn densification, d, that is calibrated with all available ice-shelf thickness data. The h_f is:

$$h_f = h_{dem} - H_i\left(1 - \frac{\rho_i}{\rho_w}\right) - d \quad (2)$$

The error in h_f is 6 m based on an uncertainty of 2 m for h_{dem}, 50 m in H_i and 2 m for the firn depth, d, which is optimized so $h_f \approx$ zero on the ice shelf proper.

Ice-shelf melt rate. Time series of surface elevation and grounding-line position allow us to calculate the ice-shelf melt rates, m_b. From the time series of height above floatation, we identify the time when h_f crosses 0 m and calculate the slope of change in elevation when ice is grounded, dh/dt_{gd}, and after ice becomes afloat, dh/dt_{fl}. A comparison of h_f with the grounding-line position helps gain confidence in the detection of the transition to flotation. The term dh/dt_{gd} is the thinning rate of grounded ice due to ice dynamics. The term dh/dt_{fl} is the thinning rate of floating ice or recently ungrounded ice, which includes dynamic thinning and ice-shelf melt. The ice-shelf melt, m_b, is deduced from the difference between these quantities:

$$\frac{dh}{dt_{gd}} = \nabla(\mathbf{u}h) + m_s \quad (3)$$

$$\frac{dh}{dt_{fl}} = [\nabla(\mathbf{u}h) + m_s + m_b]\,f \quad (4)$$

$$m_b = f\frac{dh}{dt_{fl}} - \frac{dh}{dt_{gd}}\partial \quad (5)$$

where h is the surface elevation, m_s is the surface mass balance, $\boldsymbol{u}$ is the depth-averaged velocity and $f = \rho_w/(\rho_w - \rho_i) \approx 9.33$ is a flotation factor deduced from the densities of ice and seawater. We assume that dynamic thinning does not change rapidly in space as ice ungrounds over length scales of a few ice thickness. We confirm this by verifying that the grounded ice thinning rate in a box adjacent to the 2020 grounding line is similar to that calculated in a nearby box on ice that becomes ungrounded during the observation period (Figs. 1 and 4). This Eulerian framework, based on the change in elevation at a fixed point in space, reveals how rapidly ice melts as the grounding line retreats and ice is exposed to warm ocean waters.

Data availability

All data needed to evaluate the conclusions in the paper are present in the paper and/or Supplementary Information. The CSK data (original COSMO-SkyMed product ASI, Agenzia Spaziale Italiana (2007–2020)) were provided by the Italian Space Agency (ASI) and the TDX data (original TanDEM-X product DLR (2007–2019)) by the German Space Agency (DLR). CSK data are publicly available through data grants from ASI. TanDEM-X CoSSC products were through scientific proposal OTHER0103 and are publicly available. Velocity (https://nsidc.org/data/NSIDC-0484/versions/2) and BedMachine (https://nsidc.org/data/NSIDC-0756/versions/2) data products are available as MEaSUREs products at the National Snow and Ice Data Center, Boulder CO (NSIDC). Geocoded interferograms, grounding-line positions, reference surface elevation, reference ice thickness, reference height above flotation and reference ice velocity are available at https://doi.org/10.7280/D1B114.

References

35. Rizzoli, P. et al. Generation and performance assessment of the global TanDEM-X digital elevation model. *ISPRS J. Photogramm. Remote Sens.* **132**, 119–139 (2017).
36. Padman, L., King, M., Goring, D., Corr, H. & Coleman, R. Ice-shelf elevation changes due to atmospheric pressure variations. *J. Glaciol.* **49**, 521–526 (2003).
37. Berrisford, P. et al. *The ERA-Interim Archive* Version 2.0 (ECMWF, 2011).

Acknowledgements

This work was conducted at the UC Irvine under a contract with the Cryosphere Program of NASA (17-CRYO17–0025, 80NSSC18M0083 and NNX17AI02G). E.R. acknowledges support from the NSF (F0691-04).

Author contributions

P.M. set up the CSK Antarctica experiment and acquisition plans and processed and analysed the CSK data. P.R., P.P.-I. and J.L.B.-B. processed the TDX time-tagged DEMs. P.M. and E.R. interpreted the results and wrote the manuscript. L.D. provided support with the CSK data. All authors reviewed the manuscript.

Competing interests
The authors declare no competing interests.

Additional information
Supplementary information The online version contains supplementary material available at https://doi.org/10.1038/s41561-021-00877-z.

Correspondence and requests for materials should be addressed to P. Milillo.

Peer review information *Nature Geoscience* thanks David Lilien and the other, anonymous, reviewer(s) for their contribution to the peer review of this work. Primary Handling Editor: Tom Richardson.